Korean J. Chem. Eng., 40(6), 1317-1330 (2023)
DOI: 10.1007/s11814-023-1437-8

pISSN: 0256-1115
eISSN: 1975-7220

Low-temperature catalytic hydrogen combustion over Pd-Cu/Al_2O_3: Catalyst optimization and rate law determination

Jongho Kim*, Arash Tahmasebi*,†, Jang Mee Lee*, Soonho Lee*, Chung-Hwan Jeon, and Jianglong Yu***,†**

*Chemical Engineering, University of Newcastle, Callaghan, NSW 2308, Australia
**Pusan Clean Energy Research Institute, Pusan National University, Busan 46241, Korea
***Monash University-Southeast University Joint Graduate School and Suzhou Industrial Park Monash Research Institute of Science and Technology (MSRI), Suzhou, Jiangsu 215123, China
(*Received 5 November 2022 • Revised 13 January 2023 • Accepted 5 February 2023*)

Abstract−Catalytic hydrogen combustion (CHC) is a promising technology for clean, efficient, and safe energy generation in hydrogen-fueled systems such as fuel cells and passive autocatalytic recombination. This study investigates catalytic hydrogen combustion over the Pd-Cu/Al_2O_3 catalysts at low temperatures (<125 °C) to determine the rate law using a differential fixed-bed reactor. The particle size distribution and reducibility of the catalysts were studied to investigate the influence of the catalyst composition on its reactivity. Higher reduction temperatures promoted the formation of metallic Pd, leading to improved catalytic reactivity at the optimized composition of $Pd_{0.75}Cu_{0.25}/Al_2O_3$. Furthermore, the rate law of CHC over the optimized catalyst was determined by non-linear regression based on the experimental reaction rates obtained under different partial pressures of H_2 and O_2. The Langmuir-Hinshelwood single-site mechanism was found to provide the best description of the catalytic combustion of hydrogen at low temperatures.

Keywords: Catalytic Hydrogen Combustion, Bimetallic Catalyst, Palladium, Copper, Rate Law

INTRODUCTION

Due to the strong demand for reduced greenhouse and toxic gas emissions (e.g., CO_2 and NO_x) driven by the increasingly stringent environmental regulations, H_2-fueled energy systems have attracted intense worldwide interest in academic and industrial research. Several technologies using H_2 as fuel including hydrogen gas turbines and hydrogen fuel cells have been developed to improve their performance characteristics, such as combustion efficiency, and make them more tolerant to impurities such as CO [1-17]. Conventional flame combustion in hydrogen gas turbines can lead to the thermal formation of a significant amount of NO_x, while fuel cells require 99.97% ultra-pure H_2 and the use of expensive catalysts such as Pt and Pd. Many efforts have been made to develop advanced technologies to address the abovementioned techno-economic issues (i.e., environmental issues and catalyst cost) of the H_2-fueled energy systems; in particular, catalytic combustion has been an attractive approach since it was first demonstrated by Pfefferle et al. in 1970 [18]. Catalytic combustion results in ultra-low NO_x emissions because the catalytic reaction is carried out at a lower temperature (500 °C) than the temperature at which thermal NOx begins to be generated in combustion systems (1,200 °C) [19-24]. In particular, catalytic hydrogen combustion (CHC) uses H_2 as fuel reacting with air resulting in zero carbon-based emissions due to the absence of carbon content in the reactants. CHC is an exothermic reaction of H_2 and O_2 that produces water as described by Eq. (1).

$$H_2+\frac{1}{2}O_2\rightarrow H_2O,\ \Delta H^{f,\,gas}_{T_\infty,\,H_2O}=-241.81\ \text{kJ/mol} \tag{1}$$

This gas-phase reaction is roughly equivalent to the oxygen reduction reaction in H_2 fuel cells at zero cell potential (U=0) [25]. Many researchers have investigated CHC under safe conditions such as the catalytic reaction of fuel cell anode off-gas [26-29] and passive autocatalytic recombination used in nuclear power plants [30-36], which have been used to convert the remaining hydrogen gas to water to prevent hydrogen explosions. The accumulation of unreacted hydrogen may cause the formation of combustible or explosive mixtures [37]. One of the "balance-of-plant" components in a fuel cell system is a catalytic combustor [38,39] that is used to remove unreacted H_2 and supply heat under fuel cell conditions at up to 120 °C for proton-exchange membrane fuel cells (PEMFCs). In addition, passive autocatalytic recombination removes hydrogen from the containment of a nuclear power plant to prevent hydrogen explosions. Further research is required to enhance catalytic activity and reduce the cost by modifying catalysts [40].

Furthermore, many researchers have extensively studied the physicochemical properties and catalytic activity of various catalysts. In catalysts, metallic nanoparticles are commonly combined with oxide frameworks to improve the nanoparticle thermal stability and prevent agglomeration [41]. The activities of the catalysts that have been utilized for the CHC reaction, including noble (i.e., Pd) and non-noble transition metals (i.e., Cu, Co, Ni), show a volcano-shaped curve as a function of the heat of formation per gram-atom of oxygen [42]. Pd displays the highest activity on the volcano curve for the CHC reaction, and it shows activity that is even higher than that

†To whom correspondence should be addressed.
E-mail: arash.tahmasebi@newcastle.edu.au, jianglong.yu@monash.edu
Copyright by The Korean Institute of Chemical Engineers.

of Pt. To reduce catalyst cost, extensive efforts have been made to reduce the use of the deposited noble metals (e.g., Pt and Pd) in the catalysts [29,43,44]. The effects of non-noble transition metals added to the novel metal catalysts for catalytic reactions have been widely investigated and their metal-metal interactions were shown to improve activity and selectivity [45,46]. The catalytic activity of bimetallic catalysts has also been extensively investigated with various characterization techniques including microscopy and X-ray photoelectron spectroscopy (XPS), which provide information about the catalytic particle size distribution and lattice parameters, and the valence state, respectively [35,47-49]. Lomot et al. [36,50] reported a higher catalytic activity of Pd-Ni/Al_2O_3 under dry and wet conditions at a low hydrogen concentration (0.5 vol% in the air) compared with Pd/Al_2O_3.

The effect of metal-metal interaction on CHC [35,47,48,50] has been intensively investigated; however, various non-noble transition metals and their interaction with Pd have not been examined and are not well-understood. The synergistic interactions between Pd and Cu also have been attractive in catalytic reactions, such as electrochemical reduction [51] and oxidation [52], due to the changes in the Pd-O and Cu-O binding energies with the variation of the metal d-band center, improving catalytic activity and selectivity [53]. Furthermore, several studies have reported that Pd-Cu nanoparticles were designed to enable Pd metal to act as active metal sites for dissociative hydrogen uptake and hydrogen spillover onto the Cu surface [54]. However, even though Cu and Pd have been utilized for other catalytic reactions, the effects of Cu addition on Pd for CHC and its underlying mechanism have not been thoroughly investigated.

Previous studies have reported a wide range of 1-74 kJ/mol for the activation energy of the CHC reaction [55]. Even though the kinetic parameters of various catalysts have been obtained from the literature, the rate law, which is of critical importance in catalytic reactor design, has not been determined for CHC. The rate law also provides important information, such as the required amount of catalyst, reactor volume, and the effect of the partial pressures of reactants and products for the design of catalytic reactors. Therefore, this study seeks to optimize the preparation of the Pd-Cu bimetallic catalyst on an Al_2O_3 substrate, investigate the characteristics of the catalysts using various analytical techniques, and accurately determine the rate law of the CHC reaction over the optimized catalyst.

EXPERIMENTAL

1. Catalyst Preparation

Commercial activated alumina powder (surface area: 173.3 m^2/g, Sigma-Aldrich) with particle sizes in the range of 40-160 μm was used as the catalyst support. The metal precursors for loading Pd and Cu were palladium chloride and copper (II) nitrite hydrate, purchased from Sigma-Aldrich. The total weight of the metal loaded on the support material was fixed as 1 wt% for all of the prepared catalysts. First, the support material was added to a mixture of the aqueous solution of metal precursors with distilled water. The monometallic Pd/Al_2O_3 and Cu/Al_2O_3 catalysts were prepared via the impregnation method with a certain amount of Pd or Cu metal precursor for loading 1 wt% of Pd and Cu on the support material, respectively. The bimetallic catalysts, Pd_x-Cu_{1-x}/Al_2O_3 with different elemental compositions (x=0, 0.25, 0.5, 0.75, and 1 with weight basis) were prepared by the co-impregnation method as follows. The solution was stirred overnight while adding 0.1 M HCl to retain pH 5 and was then centrifuged. The collected sample was washed with distilled water and centrifuged again. The resulting samples were dried in an oven at 100 °C overnight, calcined in air at 400 °C for 4 h, and reduced with 30 vol%H_2/N_2 at various temperatures (300, 400, 500, and 600 °C) for 3 h. Both heat treatments were at a heating rate of 10 °C/min. The catalysts prepared at the reduction temperature of 400 °C were termed "Pd_x-Cu_{1-x}/Al_2O_3", (i.e., $Pd_{0.75}Cu_{0.25}$/Al_2O_3). The catalysts prepared at different reduction temperatures after calcination have "(Rx00)" at the end of their name, where "x00" is the reduction temperature in degree Celsius (i.e., 0.75Pd0.25Cu/Al_2O_3 (R300)).

2. Catalyst Characterization

The prepared catalysts were characterized by several analytical techniques to determine their physicochemical and catalytic properties. Powder X-ray diffraction (XRD) was carried out with an Xpert pro XRD instrument (Malvern Panalytical) using Cu K alpha radiation in a Bragg-Brentano configuration for the 2θ angle range of 10-80°. Brunauer-Emmett-Teller (BET) surface areas of the support material and prepared catalysts were obtained by N_2-physisorption analysis using a Tristar 3000 instrument (Micromeritics) at 77 K. High-resolution transmission electron microscopy (HRTEM) was used to analyze the sizes of metal active sites over the catalysts with a TEM 2100 instrument (JEOL). Energy-dispersive X-ray spectroscopy (EDS) was used to analyze the metal distribution of Pd and Cu over the support material. Elemental compositions of Pd and Cu on the catalyst surface were evaluated by inductively coupled plasma mass spectrometry (ICP-MS) using an Agilent 7700 Series instrument (Agilent). Prior to the ICP-MS measurements, the samples were prepared using an SCP Science Digi PREP MS digestion block system with solutions. Temperature programmed reduction (TPR) measurements were carried out to investigate the reducibility of the various catalysts using a catalyst analyzer (BELCAL II, BEL Corp.) equipped with a thermal conductivity detector (TCD). The catalyst samples (approximately 100 mg) were loaded in a quartz tube packed with quartz wool. The loaded samples were dried under helium gas at 120 °C for 24 h and were subjected to flowing 3 vol%H_2/He at 20 mL/min in the temperature range from 20 °C to 400 °C. The TCD detects consumed hydrogen to compare the reducibility of various catalysts in this study. This temperature was chosen because it does not affect the intrinsic structure features of the catalysts (ramp: 10 °C/min). X-ray photoelectron spectroscopy (XPS) analysis was performed with the Thermo Scientific K-alpha XPS system (ThermoFisher) using Al Kα X-ray exciting electrons to obtain the oxidation state of the metal loaded on the catalysts.

3. Catalytic Reactivity Tests

Catalytic reactivity tests were carried out in a custom-designed quartz reactor over various catalysts with different elemental compositions and reduction temperatures to identify the optimal catalyst. The inner diameter and length of the quartz reactor were 10 mm and 435 mm, respectively, and the reactant mixture was 1 vol%H_2/air with a total flow rate of 200 mL/min. A 0.05 g of the

catalyst was loaded for the measurement of the kinetic parameters. The catalytic activity tests for the calcined catalysts as well as for the commercial 1Pd/Al_2O_3, purchased from Sigma-Aldrich and used as the reference, were also carried out for comparison with catalysts prepared in this study. The reaction temperature ranged from ambient to 125 °C, which is the minimum temperature to complete hydrogen conversion over the Pd-containing calcined catalysts. The product gas composition was analyzed online using an Agilent 490 Micro GC that measured the outlet concentrations of hydrogen during experiments. A thermal conductivity detector (TCD) was used in the micro-GC. Gas sample was injected into a 10 m (Molecule sieve) MS5A column (with helium as the carrier gas) and a 10 m (Polar Plot U) PPU column (with argon as the carrier gas). The column temperature during the measurements was 60 °C. Before measurements, the micro-GC was calibrated using a standard gas mixture (2.04 vol%H_2 balanced with He). The conversion rate and the reaction rate of hydrogen were calculated from the following equations:

$$X_{H_2}=\frac{C_1-C_2}{C_1} \tag{2}$$

$$-r'_{H_2}=\frac{X_{H_2}}{\Delta W/F_{H_2}}\left[\frac{mol}{g\cdot s}\right] \tag{3}$$

where X_{H_2} is the hydrogen conversion, C_1 and C_2 are the feed and outlet concentrations of hydrogen, ΔW is the weight of the catalyst loaded in the quartz reactor in g, and F_{H_2} is the initial flow rate of hydrogen in mol/s.

4. Rate Law Determination

The partial pressure effects of H_2 and O_2 were studied under isothermal and differential conditions over the catalyst with the optimized composition. The total flow rate and catalyst weight were 200 mL/min and 0.05 g, respectively, consistent with the catalyst optimization experiments. The H_2 and O_2 concentrations ranged from 0.5 to 7 vol% and from 1.2 to 7 vol%, respectively. The experiments with varying H_2 concentrations were carried out under an O_2 concentration of 1.2 vol%, while those with varying O_2 concentration were performed under an H_2 concentration of 6%, thus covering both H_2-lean and H_2-rich conditions.

The rate law model can be determined by a non-linear regression based on the general form of the rate law equation and using the recorded changes in reaction rates as a function of the partial pressures of reactant gases. In this study, the equation includes the hydrogen partial pressure term in both the numerator and denominator because the CHC reaction rate first increases and then decreases with increasing hydrogen partial pressure. On the other hand, the oxygen partial pressure term is found only in the numerator due to the monotonically increasing reaction rates of CHC with increasing oxygen partial pressure. Then, the empirical form given by kinetic model 1 (Eq. (4)) was determined with the rate law parameters and the parameters obtained by the non-linear regression method [56].

Kinetic model 1: Empirical form

$$r'_{H_2O}=\frac{aP_{O_2}^{\alpha_1}P_{H_2}^{\alpha_2}}{1+bP_{H_2}^{\beta_1}} \tag{4}$$

where P_{H_2} and P_{O_2} represent the partial pressures of H_2 and O_2 in bar, and a, b, α_1, α_2, and β_1 are the rate law parameters in the general form of the rate law equation.

Furthermore, several heterogeneous catalysis kinetic models including the Langmuir-Hinshelwood (L-H) and Eley-Rideal (E-R) mechanisms depend on the chemisorption of reactants during the reaction process [57]. The E-R mechanism describes the surface reaction between an adsorbed reactant (i.e., H_2, O_2) over the catalyst and another reactant from the bulk stream. In contrast, the L-H mechanism describes the surface reaction between two reactant gas molecules adsorbed on the catalyst active sites. The four possible kinetic models (kinetic models 2-5) for CHC are described by Eqs. (5)-(8):

Kinetic model 2: E-R mechanism (H_2 adsorbed)

$$r'_{H_2O}=\frac{kK_1P_{H_2}P_{O_2}}{1+K_1P_{H_2}+K_2P_{O_2}} \tag{5}$$

Kinetic model 3: E-R mechanism (O_2 adsorbed)

$$r'_{H_2O}=\frac{kK_2P_{H_2}P_{O_2}}{1+K_1P_{H_2}+K_2P_{O_2}} \tag{6}$$

Kinetic model 4: Single site L-H mechanism (H_2 and O_2 adsorbed on the same site)

$$r'_{H_2O}=\frac{kK_1K_2P_{H_2}P_{O_2}}{(1+K_1P_{H_2}+K_2P_{O_2})^2} \tag{7}$$

Kinetic model 5: Duel site L-H mechanism (H_2 and O_2 adsorbed on two sites)

$$r'_{H_2O}=\frac{kK_1K_2P_{H_2}P_{O_2}}{(1+K_1P_{H_2})(1+K_2P_{O_2})} \tag{8}$$

where k is the kinetic reaction constant in $\mu mol\cdot g^{-1}\cdot s^{-1}$, K_1 and K_2 indicate the adsorption constant of H_2 and O_2 in bar^{-1}, and P_{H_2} and P_{O_2} are the partial pressures of H_2 and O_2 in bar. The two adsorption constants and rate constant in each kinetic equation were calculated as a function of reaction temperature based on the Arrhenius and van't Hoff equations [57].

$$k=Ae^{-E_a/RT} \tag{9}$$

$$K_i=A_ie^{-E_i/RT} \tag{10}$$

where E_a is the activation energy of the surface reaction and E_i is the activation energy of the adsorption of gas i (H_2 and O_2); A and A_i are the pre-exponential factors of the surface reaction and adsorption of gas i, respectively.

RESULTS AND DISCUSSION

1. Influence of Catalyst Composition on Hydrogen Combustion Reactivity

In this section, the catalytic activity of the reduced catalysts and their physicochemical and catalytic properties as analyzed by XRD, TEM, and XPS techniques are presented and compared to those of the calcined catalysts discussed in the previous section. Table 1 presents the physicochemical properties of the catalysts reduced at 400 °C, including the BET surface area, active metal mean size,

Table 1. Physicochemical and catalytic properties of various reduced catalysts with different elemental compositions of Pd and Cu

Catalyst sample	BET surface area (m^2/g)	Active metal size[a] [nm]	Nominal metal composition [wt%]		Actual metal composition[b] [wt%]		T_{90} [°C]
			Pd	Cu	Pd	Cu	
Pd/Al_2O_3 (R)	160.26	6.24	1.00	0	1.00	0	62
$Pd_{0.75}Cu_{0.25}/Al_2O_3$ (R)	165.96	5.72	0.75	0.25	0.73	0.24	31
$Pd_{0.5}Cu_{0.5}/Al_2O_3$ (R)	165.12	6.34	0.5	0.5	0.48	0.43	52
$Pd_{0.25}Cu_{0.75}/Al_2O_3$ (R)	166.84	7.11	0.25	0.75	0.21	0.59	75
Cu/Al_2O_3 (R)	169.56	5.39	0	1.00	0	0.96	80

[a]Analyzed by TEM.
[b]Analyzed by ICP-MS.

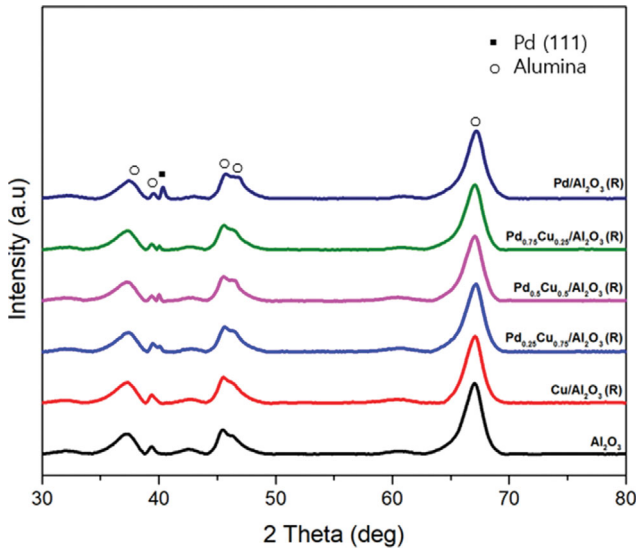

Fig. 1. XRD measurements of reduced Pd-Cu supported alumina catalysts.

and metal composition as well as the T_{90} defined as the reaction temperature at which conversion reaches 90% of the total hydrogen conversion.

The BET surface areas of the reduced catalysts are lower than that of the support material, indicating that the impregnated metal nanoparticles may have blocked some pores of the support material. Generally, the BET surface area for catalysts with a higher amount of Pd was lower than that of the Cu catalyst, which was attributed to the higher crystal size of Pd than Cu.

The XRD patterns of the catalysts and the support material are presented in Fig. 1. A slight peak representing Pd (111) was observed at 40.3° in the XRD pattern of Pd/Al_2O_3. While no obvious peaks were observed for the Cu-containing catalysts due to the small amount loaded and much smaller particle size of Cu in the catalysts compared to Pd, relatively clear peaks for Pd (111) were found for the Pd-containing catalyst samples. The XRD measurements of the calcined catalysts are provided in the Supplementary Material, and the patterns of the calcined Pd-containing catalysts do not show Pd (111) compared to the XRD patterns of the reduced catalysts, indicating that converted metal on the catalysts after reduction process.

The TEM images and particle size distribution histograms of the reduced catalysts with different elemental compositions of Pd and Cu are presented in Fig. 2. The TEM images show that, generally, active metal particles are relatively well distributed on the catalyst surface (darker areas show active metal particles). The order of active metal particle sizes is as follows: $Pd_{0.25}Cu_{0.75}/Al_2O_3$ (R) (7.00 nm)>$Pd_{0.5}Cu_{0.5}/Al_2O_3$ (R) (6.41 nm)>Pd/Al_2O_3 (R) (6.24 nm)>$Pd_{0.75}Cu_{0.25}/Al_2O_3$ (R) (5.72 nm)>Cu/Al_2O_3 (R) (5.39 nm). Many researchers presented that a smaller active metal size generally results in higher catalytic reactivity in many catalytic reactions such as CO oxidation [58] and room-temperature CHC [48]. However, the findings of this study, as presented in Table 1, do not show a significant difference in the active metal size of different catalysts. Therefore, active metal size does not seem to be a dominant factor in catalyst reactivity.

It has been also reported that a strong metal-support interaction effect improves the catalytic reactivity when noble metal-based catalysts are prepared using reducible oxides such as TiO_2 [58]. Metal-support interactions are classified as either weak (e.g., with SiO_2 and Al_2O_3), medium (with zeolites), or strong (e.g., with TiO_2) [59]. The acidic conditions during the catalyst preparation will endow the non-reducible catalysts with reducibility by generating defects at the surface, which promotes metal-support interactions [59].

The d-spacings of the catalysts with different elemental compositions are as follows: Pd/Al_2O_3 (0.224 nm); $Pd_{0.75}Cu_{0.25}/Al_2O_3$ (0.223 nm); $Pd_{0.5}Cu_{0.5}/Al_2O_3$ (0.222 nm); $Pd_{0.25}Cu_{0.75}/Al_2O_3$ (0.219 nm); Cu/Al_2O_3 (0.215 nm). The decreasing lattice parameter results from the interpenetration of Cu which are smaller than palladium [60]. The HRTEM images of reduced $Pd_{0.75}Cu_{0.25}/Al_2O_3$ and Pd/Al_2O_3 are provided in Fig. 3. This is also in agreement with the XRD profile of Pd/Al_2O_3. Literature reports a Cu (111) lattice fringe of 0.21 nm [61], which is similar to that of Cu/Al_2O_3 obtained in this study. Furthermore, changes in the lattice fringe sizes indicate the formation of alloys as inferred by the reduced d-spacing sizes compared to that of Pd [62]. Zheng et al. [63] also reported the lattice spacing distances of 0.223 and 0.224 nm for $Pd_{62.5}Cu_{37.5}$ (atomic ratio) and pure Pd, respectively. The reduced d-spacing size was reported as evidence of Pd-Cu alloyed nanostructure formation. In addition, the uniform distribution of both Pd and Cu in bimetallic nanoparticles in the EDS mapping images in Fig. 8 confirms the formation of alloyed nanostructures and the chemi-

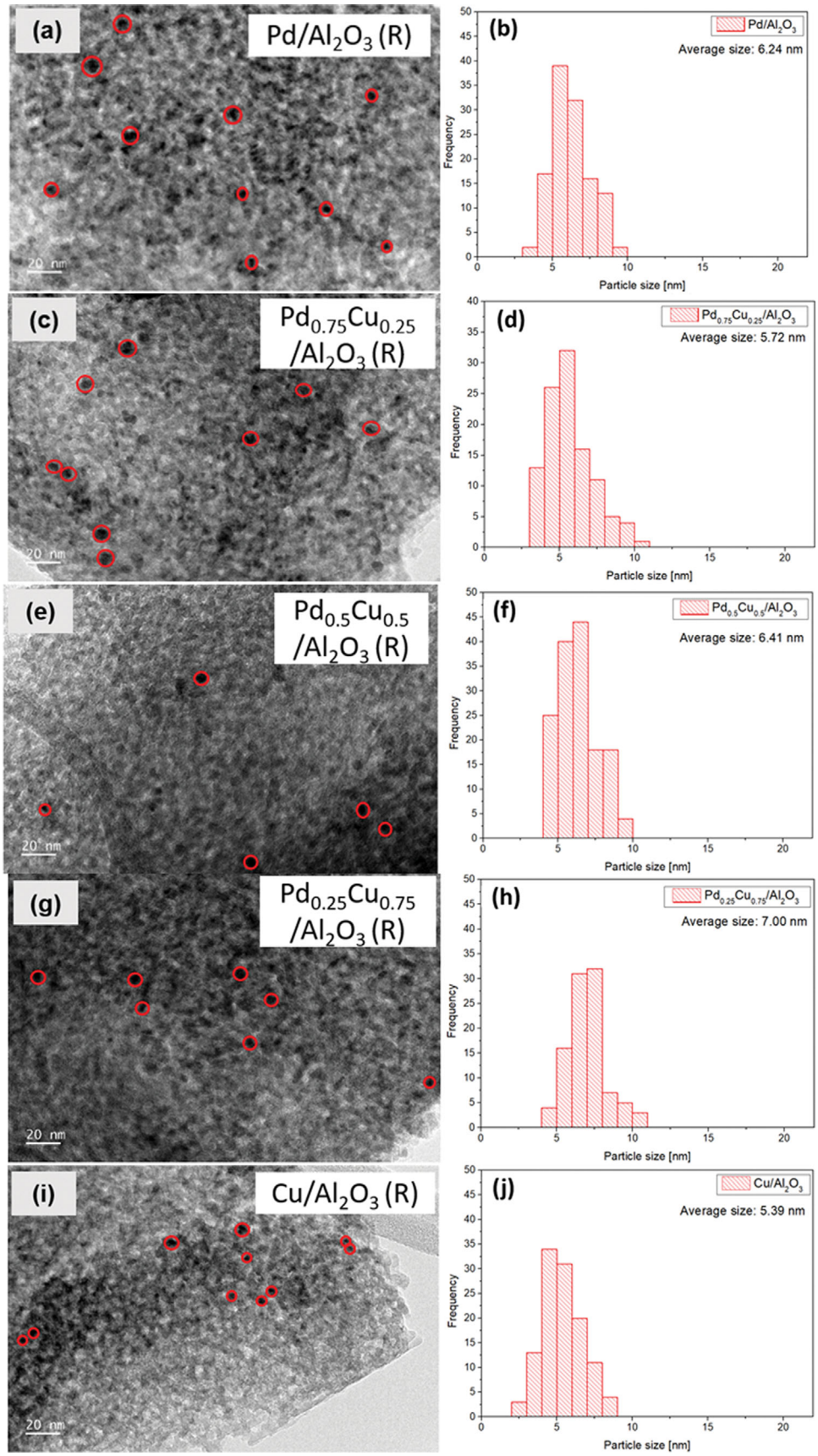

Fig. 2. TEM images ((a), (c), (e), (g), (i)) and the particle size distributions ((b), (d), (f), (h), (j)) of Pd/Al_2O_3 (R), $Pd_{0.75}Cu_{0.25}/Al_2O_3$ (R), $Pd_{0.5}Cu_{0.5}/Al_2O_3$ (R), $Pd_{0.25}Cu_{0.75}/Al_2O_3$ (R), and Cu/Al_2O_3 (R) (Red circles represent active metal particles).

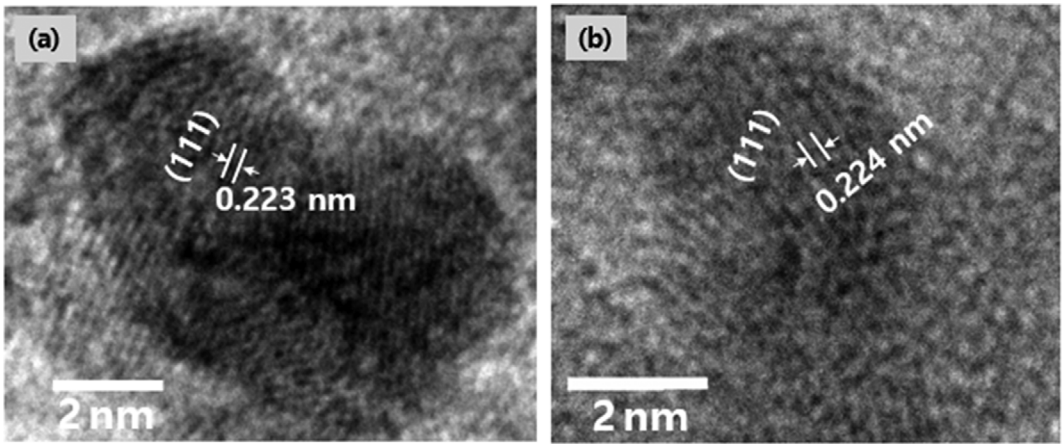

Fig. 3. HRTEM images of alumina supported (a) $Pd_{0.75}Cu_{0.25}/Al_2O_3$ (R) and (b) Pd/Al_2O_3 (R) nanoparticles.

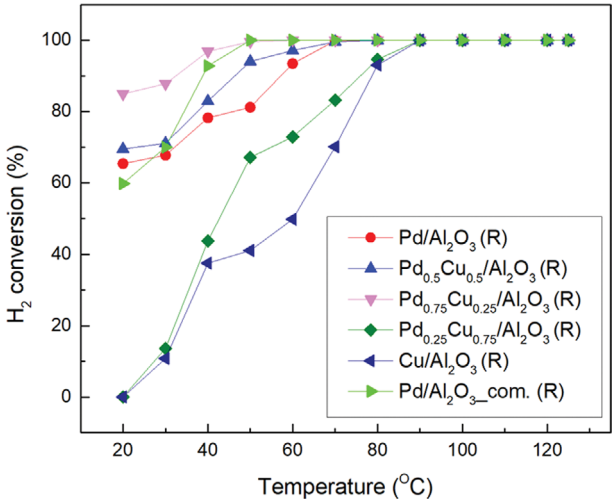

Fig. 4. Hydrogen conversion over Pd_x-Cu_{1-x}/Al_2O_3 catalysts with different metal compositions reduced at 400 °C as a function of the reaction temperature.

cal composition of bimetallic nanoparticles.

Fig. 4 shows the hydrogen conversion during CHC as a function of catalyst composition and reaction temperature. The $T_{1/2}$ (the temperature where hydrogen conversion reached 50%) of calcined Pd and Cu was measured at approximately 75 and 125 °C, respectively, which indicates their poorer activity than the reduced phases. The greatest conversion was recorded for $Pd_{0.75}Cu_{0.25}/Al_2O_3$ (R) followed by $Pd_{0.5}Cu_{0.5}/Al_2O_3$ (R). Even though the hydrogen conversion over $Pd_{0.25}Cu_{0.75}/Al_2O_3$ (R) and Cu/Al_2O_3 (R) was zero at ambient temperature, they gradually increased with increasing reaction temperature and reached complete conversion at 90 °C. Also, the profile of hydrogen conversion over commercial Pd/Al_2O_3 (R), which was reduced, is provided for comparison with the prepared catalysts. It converted approximately 60% of hydrogen at 20 °C, which is lower than the hydrogen conversion of the three better catalysts. However, it showed a higher conversion of hydrogen at 40 °C, which was interestingly still poorer than that over $Pd_{0.75}Cu_{0.25}/Al_2O_3$ (R). In contrast, the hydrogen conversion of the catalysts with a Pd content of higher than 0.25 wt% was higher than 60% at 20 °C and reached complete conversion at 70 °C. The reduction process converted the oxide to the metal phase, leading to higher catalytic activity [64]. In this study, the reduced Cu/Al_2O_3 catalyst showed a comparable reactivity to the commercial Pd/Al_2O_3. Cu played an active site for the reaction, and it became more dominant at higher temperatures. The catalytic activity of Cu or CuOx during hydrogen combustion has been reported to be fairly high, with $T_{1/2}$ of Cu and CuO of around 250 °C [29] and 200 °C [42], respectively.

Interestingly, the catalytic reactivity of $Pd_{0.75}Cu_{0.25}/Al_2O_3$ and $Pd_{0.5}Cu_{0.5}/Al_2O_3$ shown in Fig. 4 is higher than that of Pd/Al_2O_3 even though their Pd loadings were lower, which is also reflected in the decrease in the T_{90} temperature provided in Table 1. Considering the above-mentioned d-spacings of the Pd-Cu catalysts, the improved catalytic activity of bimetallic catalysts compared to Pd and Cu catalysts can be attributed to the formation of alloys [63]. Several studies on other catalysis reactions, such as oxygen reduction reactions, have shown that the formation of a Pd-Cu alloy improves the catalytic reactivity. This may stem from the formation of a chemically disordered phase through the alloying process [53, 65]. The Pd-Cu alloy formation has been reported to have a chemically ordered and body-centered cubic (BCC) structure, rather than a face-centered cubic (FCC) structure, in the absence of Cu [53].

The TPR results for the catalysts are presented in Fig. 5. The programmed temperature was varied from 20 °C to 400 °C to investigate the reducibility of the catalysts without any changes in their chemical composition due to the additional thermal decomposition above 400 °C. Both the calcination and reduction during the sample preparation in this study were conducted at 400 °C.

For all the reduced catalyst samples, the TPR profiles were deconvoluted into three different curves. Table 2 presents the temperatures and integrated areas of peaks fitted to the TPR profiles in Fig. 5. The peak areas represent the relative amount of H_2 consumed. It was observed that the reduction over the Pd-containing catalysts started at 20 °C, while the reduction over Cu/Al_2O_3 commenced at approximately 80 °C, indicating that at low temperatures it was easier to reduce Pd than Cu. The peak temperatures of the first reductions over Pd/Al_2O_3 and Cu/Al_2O_3 were 190.3 °C and 201.5 °C,

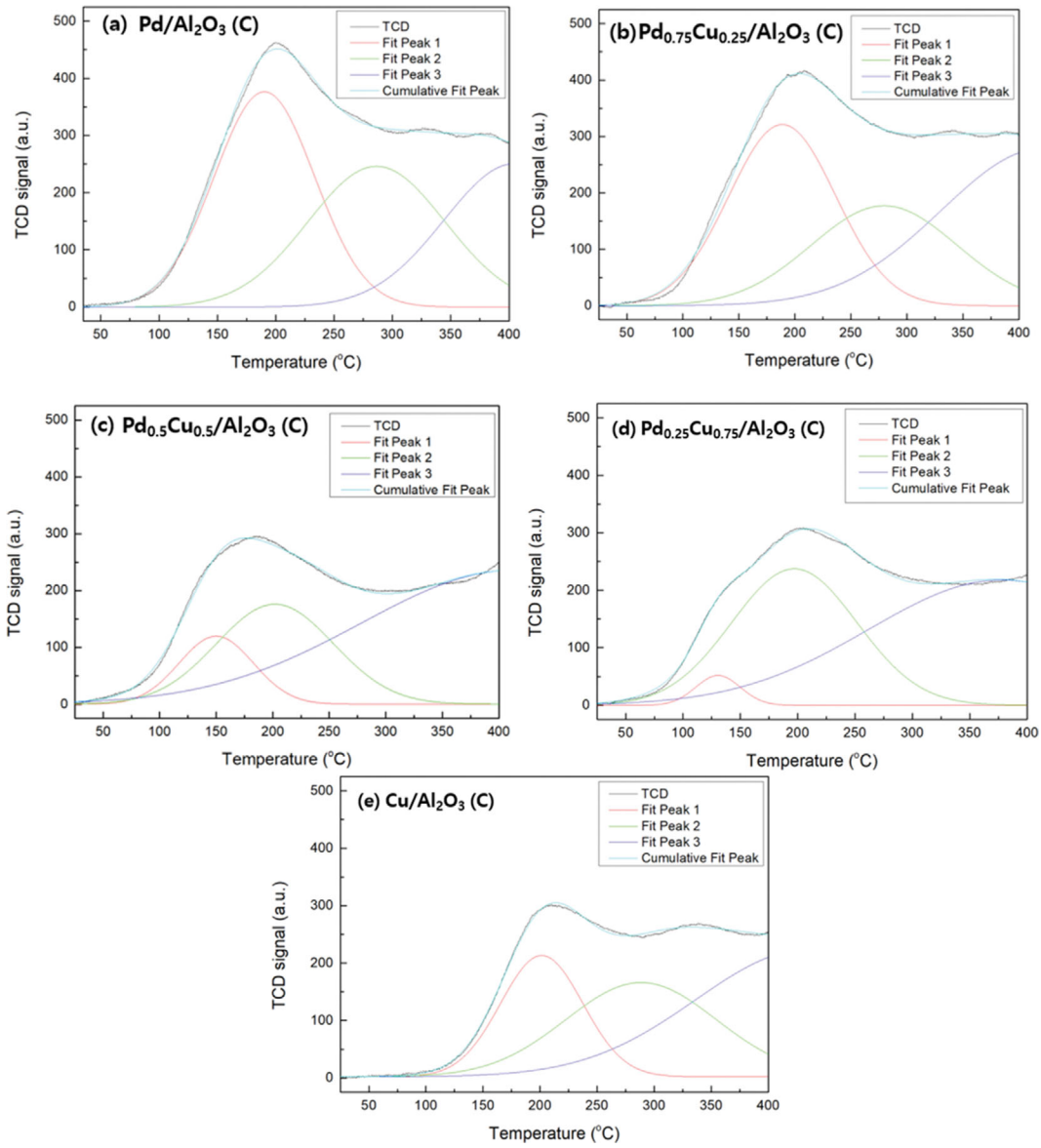

Fig. 5. Profiles for temperature-programmed reduction of calcined Pd_x-Cu_{1-x}/Al_2O_3 catalysts with different metal compositions.

Table 2. TPR peak analysis of the calcined Pd-Cu catalysts

Sample	Peak 1		Peak 2		Peak 3		Total consumed H_2 [mmol/g]
	Peak temp. [°C]	Consumed H_2 [mmol/g]	Peak temp. [°C]	Consumed H_2 [mmol/g]	Peak temp. [°C]	Consumed H_2 [mmol/g]	
Pd/Al_2O_3	190.3	0.55	286.4	0.378	405.1	0.085	1.013
$Pd_{0.75}Cu_{0.25}/Al_2O_3$	188.8	0.585	279.7	0.382	422.1	0.095	1.062
$Pd_{0.5}Cu_{0.5}/Al_2O_3$	150.0	0.41	201.9	0.313	413.9	0.078	0.801
$Pd_{0.25}Cu_{0.75}/Al_2O_3$	130.0	0.609	195.4	0.267	382.7	0.074	0.95
Cu/Al_2O_3	201.5	0.321	288.6	0.291	434.5	0.058	0.67

and the integrated area of the first reduction peak of Pd/Al_2O_3 was approximately twice that of Cu/Al_2O_3. While all peak temperatures of Cu/Al_2O_3 are higher than Pd/Al_2O_3, it is important to note that the temperatures of the first and second peaks for the Pd-Cu bimetallic catalysts decreased with a greater Cu addition and were lower than Pd/Al_2O_3. Fig. 5 also shows that the reduction continued beyond 400 °C. Similar results were reported by Liu et al. [66] from TPR analysis of the Pd-Cu bimetallic catalysts. The reduc-

tion behavior of catalysts depends on several factors, such as surface area and porosity, H_2 concentration, and reduction time. The consumed H_2 of the first reduction peaks of the bimetallic catalysts shows relatively larger variation between the catalysts with different metal compositions and shows a decreasing trend at lower Pd content. Generally, the consumed H_2 of the second and third peaks of Cu/Al_2O_3 and the Pd-Cu bimetallic catalysts were greater than those of the first curves of Pd/Al_2O_3, indicating a greater contribution to the reduction of these catalysts at higher temperatures compared to the pure Pd catalyst. Furthermore, the total consumed H_2 of the reduction curves during TPR tests were in the following order: $Pd_{0.75}Cu_{0.25}/Al_2O_3$>$Pd/Al_2O_3$>$Pd_{0.5}Cu_{0.5}/Al_2O_3$>$Pd_{0.25}Cu_{0.75}/Al_2O_3$>$Cu/Al_2O_3$. The $Pd_{0.75}Cu_{0.25}$ catalyst with the greatest Pd content showed the best performance. Lesiak et al. [67] reported a larger reduction curve with Cu addition on the TPR profile, which was attributed to the formation of Pd-Cy alloy. The reduction of mixed oxides can lead to the formation of alloys with different compositions. The formation of Pd-Cu alloys was also reported by X-ray absorption spectroscopy and X-ray photoelectron spectroscopy [67]. As an electron donor, Cu promotes the chemisorption of H_2 by Pd. In addition, Cu ion also reduces and contributes to hydrogen consumption. Compared to Pd/Al_2O_3, the improved catalytic activity of $Pd_{0.75}Cu_{0.25}/Al_2O_3$ may be caused by the smaller active metal particle size and higher reducibility as determined by TEM and TPR, respectively. Thus, these results show that the optimal Pd to Cu mass ratio is 3 : 1.

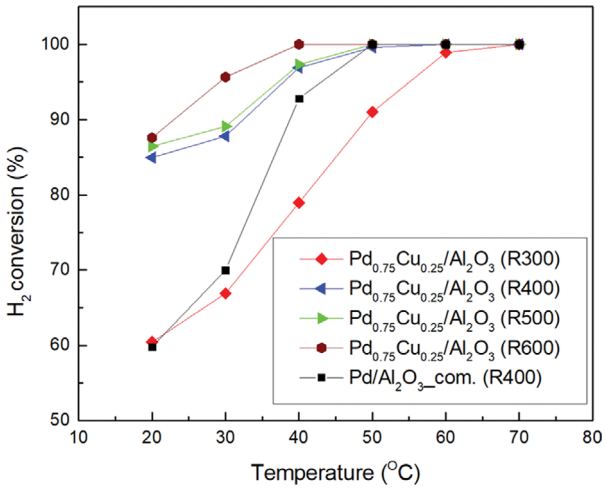

Fig. 6. Hydrogen conversion over the $Pd_{0.75}Cu_{0.25}/Al_2O_3$ catalysts as a function of reduction temperature.

2. Impact of the Catalyst Reduction Temperature on Hydrogen Combustion Reactivity

Following the optimization of the elemental composition of the

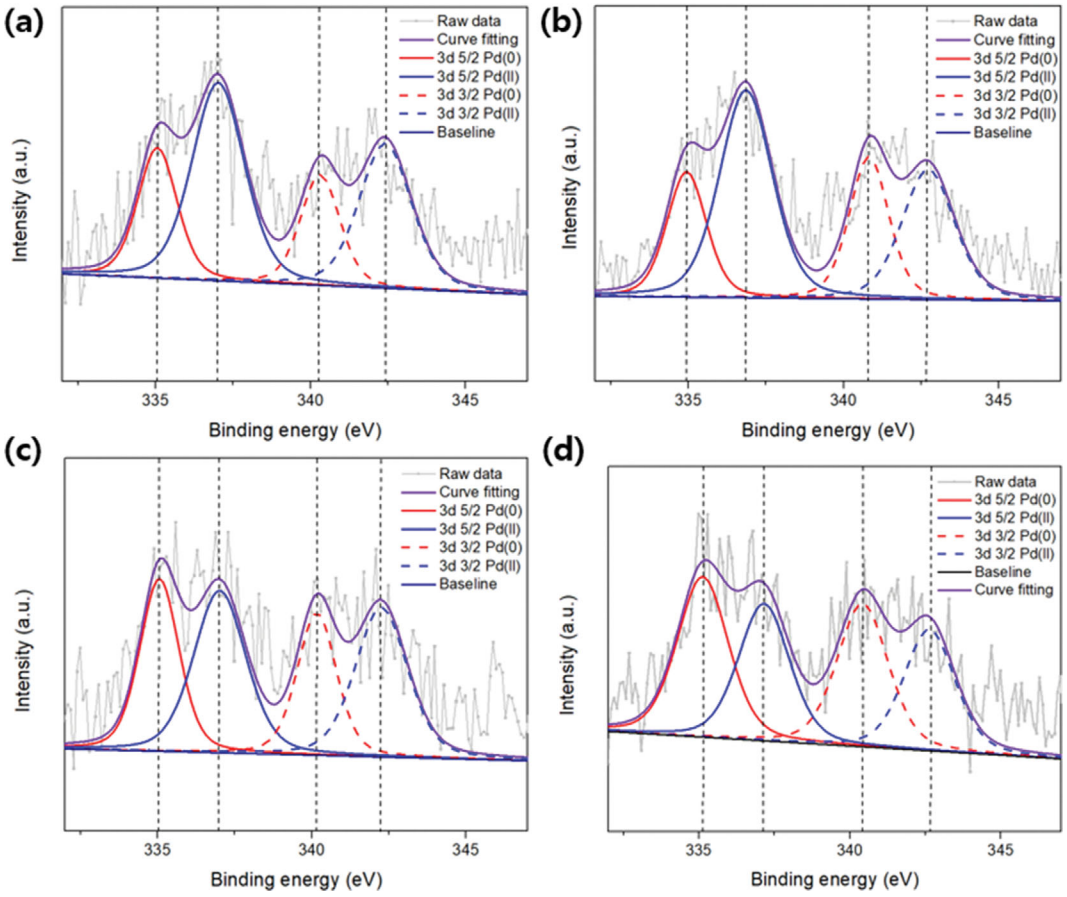

Fig. 7. XPS measurements of reduced $Pd_{0.75}Cu_{0.25}/Al_2O_3$ catalysts obtained using different reduction temperatures: (a) 300 °C; (b) 400 °C; (c) 500 °C; (d) 600 °C.

catalyst discussed above, the impact of reduction temperature on the catalyst properties and performance was investigated. For this purpose, the optimized $Pd_{0.75}Cu_{0.25}/Al_2O_3$ catalyst was used. Fig. 6 shows the influence of the reduction temperature of $Pd_{0.75}Cu_{0.25}/Al_2O_3$ catalyst on its hydrogen conversion reactivity. Below the combustion temperature of 60 °C, the catalyst reduced at 300 °C shows a very low hydrogen conversion. At 20 °C, the difference in hydrogen conversion between $Pd_{0.75}Cu_{0.25}/Al_2O_3$ (R300) and the other catalysts is approximately 0.25. The catalysts reduced at 400 °C and 500 °C are quite similar, while reduction at 600 °C led to the highest hydrogen conversion, particularly at lower temperatures. These results show that, overall, the catalytic activity at lower temperatures increases with increasing the catalyst reduction temperature.

The commercial Pd/Al_2O_3 (R) was also compared to the $Pd_{0.75}Cu_{0.25}/Al_2O_3$ catalysts reduced at different temperatures. It was observed that the hydrogen conversion of the commercial catalyst was higher than $Pd_{0.75}Cu_{0.25}/Al_2O_3$ (R300) but lower than the other catalysts reduced at higher temperatures below 50 °C. Even though the elemental composition of the catalyst significantly affects the catalytic activity of Pd-Cu catalysts, the reduction temperature was more dominant to compare catalytic activity between $Pd_{0.75}Cu_{0.25}/Al_2O_3$ (R300) and the commercial Pd/Al_2O_3 (R).

XPS analysis was used to determine the oxidation states of the metallic species on the catalyst surface, particularly for Pd which plays the dominant catalytic role during CHC (see Fig. 7). The intensity of the Cu satellites (the maximum amount of loaded Cu was 0.75 wt% in this study) was insufficient for the identification of the chemical species from XPS analysis [68]. The binding energies of metallic Pd and Pd^{2+} (oxide phase) were 335 eV, 336.7 eV for Pd $3d_{5/2}$, and 341 and 342 eV for Pd $3d_{3/2}$ presented in Table 3.

The ratios of metallic Pd to the total Pd for all catalyst samples as a function of reduction temperature were calculated from the areas under the deconvoluted curves obtained from the XPS spectra and are summarized in Table 4. The full width at half maximum (FWHM) for metallic Pd and Pd^{2+} was set according to the literature [48]. The ratios of Pd^0/Pd_{total} for the various reduction temperatures were in the following order: 34.59% (R300)<37.36% (R400)<43.17% (R500)<43.25% (R600). Generally, a higher reduction temperature leads to a higher Pd^0/Pd_{total} ratio, indicating that a larger amount of the metal phase converted from the oxide phase promoted catalytic reactivity. These results are in agreement with the literature [48]. From these XPS measurements, it should be noted that the prepared catalysts contain the oxide phases with part of alloyed metal that was proved previously by the size of fringe from the TEM results.

Table 3. Binding energy in the XPS spectra for Pd

	$3d_{5/2}$ [eV]	$3d_{3/2}$ [eV]
Pd(0)	335	341
Pd(II)	336.7	342

The reactivity of the catalysts prepared at different reduction temperatures accords with the active metal particle sizes listed in Table 4. The active metal particle sizes of the catalyst samples are as follows: 9.82 nm (R300)>5.72 nm (R400)>5.10 nm (R500)>4.09 nm (R600). Among the catalysts examined in this study, 0.75Pd0.25Cu/Al_2O_3_red600 had the smallest active metal size and the highest Pd^0/Pd_{total} ratio, as well as the highest catalytic reactivity. The similarity of hydrogen conversion from R400 and R500 may be strongly affected by their active metal sizes, which have the closest values when comparing other sizes. The particle size of active metal sites decreases with the increase in reduction temperature, which may be caused by modified Al_2O_3 from reduction [59]. Reduction by the hydrogen gas at high temperatures (i.e., >500 °C) will modify the support and change the metal-support interactions when the catalyst is prepared in acidic conditions [59]. Therefore, the smaller particle sizes of Pd and Cu that eventually lead to improved catalytic activity during hydrogen oxidation may be attributed to the strong metal-support interactions because the catalyst preparation is carried out at pH 5 through the addition of HCl [59]. It leads to the increase in the metal-support interactions, which was attributed to reduced particle sizes of Pd and Cu by decreasing the metal-metal interactions. It has been extensively reported that the smaller particle size of active metal sites improves catalytic activity during heterogeneous catalysis, such as CHC [48] and CO oxidation [48, 58]. Furthermore, the increase in the oxidation state of the active metal by reduction leads to higher catalytic activity since the nature of reduction is to convert metal ions to metal (i.e., Pd^{2+} to Pd^0). The optimal temperature to achieve the smallest particles was 600 °C. Higher temperatures of about 700 °C have been reported to lead to particle agglomeration [58].

3. Stability and Rate Law Determination of the Optimized Catalyst

In the previous sections, the influence of synthesis conditions, including the metal composition and reduction temperature, on catalyst reactivity during hydrogen combustion profiles were described. In this section, the optimized catalyst, which is $Pd_{0.75}Cu_{0.25}/Al_2O_3$ (R600), was used to conduct stability tests. In addition, catalytic reactivity tests were carried out at different partial pressures of H_2 and O_2 for rate law determination. The stability tests were car-

Table 4. Pd 3d spectra measurements and active metal particle sizes of the reduced $Pd_{0.75}Cu_{0.25}/Al_2O_3$ catalysts prepared at different reduction temperatures

	Area_Pd^0	Area_Pd^{2+}	Area_Pd_{total}	Pd^0/Pd_{total} [%]	Active metal size [nm][a]
R300	1,385.98	2,620.96	3,706.60	34.59	9.82
R400	2,176.06	3,647.97	5,002.75	37.36	5.72
R500	1,516.12	1,995.60	3,162.75	43.17	5.10
R600	1,631.92	2,141.15	3,348.15	43.25	4.09

[a]Analyzed by TEM.

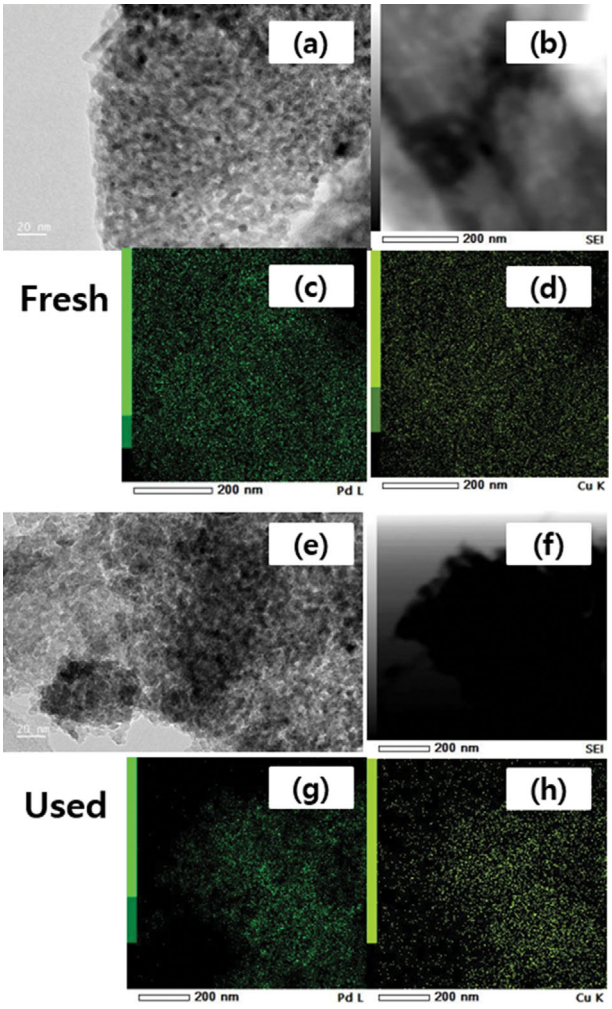

Fig. 8. TEM images ((a) and (e)) and EDS maps for the optimized catalyst sample, $Pd_{0.75}Cu_{0.25}/Al_2O_3$ (R600): ((b) and (f)) TEM images for EDS detection; Pd and Cu of the fresh ((c) and (d)) and used ((g) and (h)) samples, respectively.

ried out for 40 h to investigate the morphological changes of the catalyst as a function of reaction time. The mass of the catalyst sample was 50 mg, and the outlet hydrogen concentration was measured every hour. Complete conversion of hydrogen over the optimized catalyst was achieved for the 40 h duration of the tests. Fig. 8 shows the TEM images (100k magnification) and EDS mapping of Pd and Cu for the fresh and used catalysts after the reaction for 40 h. No significant morphological differences between the fresh and used catalysts were observed, except for some particle agglomeration as shown in Fig. 8(e)-(h).

The effects of the H_2 and O_2 partial pressures on the rate of hydrogen combustion reaction were investigated using packed-bed experiments using constant total gas flow rate and catalyst weight in the differential reactor with varying partial pressure of H_2 and O_2. Fig. 9 shows the changes in the reaction rate profiles as a function of H_2 and O_2 partial pressures and reaction temperature. At a constant O_2 concentration, the highest reaction rate was recorded at an H_2 partial pressure of 0.01 bar at 20 °C and 0.02 bar of H_2 at higher temperatures. Increasing the partial pressure of hydrogen, particularly to values higher than 0.02 bar, reduced the reaction rate. Furthermore, higher temperatures promoted the reaction rate. Except for the reaction rates at 20 °C, the reaction rates had a maximum value where the partial pressure of H_2 was 0.02 bar. At 0.02 bar of H_2 partial pressure, the equivalent ratio of H_2 and O_2 was 1.67 : 1 (H_2 : O_2), which was lower than the stoichiometric ratio (H_2 : O_2=2 : 1). When a higher ratio of H_2 gas was injected, a reduced reaction rate was recorded.

The CHC reaction rates with increasing O_2 partial pressure and at a constant hydrogen concentration were similar at 20 °C and 30 °C, while those with 0.04 bar of O_2 are lower. Further increase in the partial pressure of O_2 led to a relatively continuous increase in the reaction rate. As the partial pressure of H_2 increases under the constant O_2 concentration, it is expected that the reaction order decreases from a positive value to zero. At low partial pressures, the H_2O formation rate increases more rapidly with O_2 pressure, while at higher partial pressures of H_2, the effect of O_2 on the H_2O formation rate is less pronounced. The reaction rates increased monotonically with the partial pressure of H_2 and O_2 in the temperature range of 20-60 °C.

Based on Eq. (4), the rate law parameters were obtained by non-linear regression using the Levenberg-Marquardt algorithm,

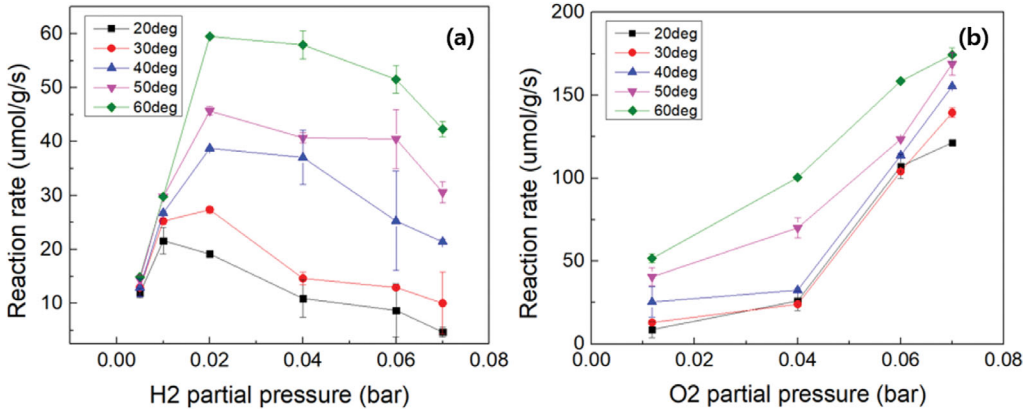

Fig. 9. Reaction rates of hydrogen over $Pd_{0.75}Cu_{0.25}/Al_2O_3$_red600 at different temperatures as a function of (a) partial pressure of hydrogen while P_{O_2} is held constant at 0.012 bar, and (b) partial pressure of oxygen while P_{H_2} is held constant at 0.06 bar.

Table 5. CHC rate law parameters over the optimized catalyst for kinetic models 1-a and 1-b

	a	b	α_1	α_2	β_1	R^2
Kinetic model 1-a	30.66	0.12	0.75	1.43	2.42	0.990
Kinetic model 1-b	35.81	0.22	1	1.5	2.5	0.958

and the parameters calculated for CHC over the optimized catalyst are presented in Table 5. The parameters of the kinetic model 1-a were calculated by the above method, while for kinetic model 1-b the parameters were recalculated with the determined reaction orders selected as the integers closest to those calculated from Eq. (4). With more experimental data points, the reaction orders are expected to be the closest integers [69], so the kinetic model 1-b may be the final form of the empirical rate law if more experiments under different partial pressures of H_2 and O_2 are carried out.

Various heterogeneous catalysis kinetic models were also employed to determine the most suitable rate law. The calculated parameters of the four models determined by the same algorithm are given in Table 6. Overall, the R^2 values suggest a good fit for all four models; nevertheless, kinetic model 4 (L-H single site) has the highest R^2 value of 0.967 as well as the highest kinetic constant.

$$r'_{H_2O}=\frac{70.32P_{H_2}P_{O_2}}{(1+0.37P_{H_2}+0.14P_{O_2})^2} \quad (11)$$

Eq. (11) is the best theoretical rate law (L-H single site) with the highest accuracy (R^2=0.967). r'_{H_2O} is a reaction rate of H_2O formation in μmol·g^{-1}·s^{-1}, and P_{H_2} and P_{O_2} are partial pressures of H_2 and O_2 in bar. The reaction rates calculated by various kinetic models are compared to the experimentally measured reaction rates in Fig. 10. The dashed line represents the y=x line. Fig. 10 shows that the experimental and calculated results were in good agreement, indicating the high accuracy of the CHC rate law obtained in this study.

Based on the kinetic models investigated in this study, the reaction mechanism of CHC over the optimized alumina-supported Pd-Cu catalyst was proposed based on the L-H single-site mechanism. The reaction steps including the adsorption of reactants, surface reaction, and desorption of the product are as follows:

$$H_{2(g)}+M_{(s)}\leftrightarrow 2H_{ad} \quad (12)$$

$$O_{(2(g)}+M_{(s)}\leftrightarrow 2O_{ad} \quad (13)$$

$$H_{ad}+O_{ad}\leftrightarrow OH_{ad} \quad (14)$$

$$OH_{ad}+H_{ad}\leftrightarrow H_2O_{ad} \quad (15)$$

$$OH_{ad}+OH_{ad}\leftrightarrow H_2O_{ad}+O_{ad} \quad (16)$$

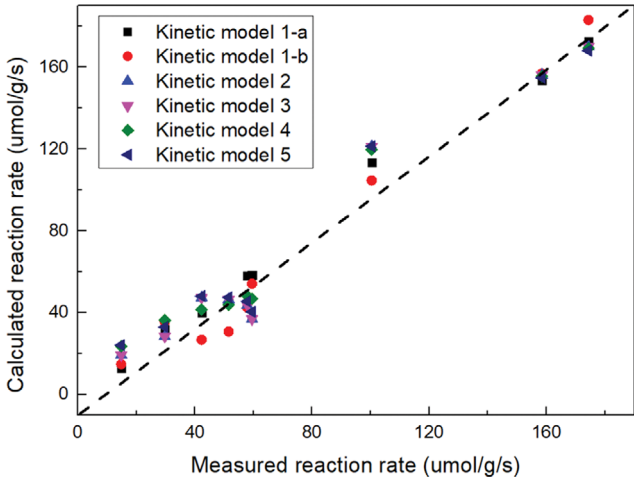

Fig. 10. Comparison between the CHC reaction rates obtained experimentally and calculated using various kinetic models.

$$H_2O_{ad}\leftrightarrow H_2O_{bulk} \quad (17)$$

where $M_{(s)}$ represents a vacant Pd or Cu active site. The reactant gases adsorb on either Pd or Cu (reactions 12 and 13). Moreover, Jones and Nevell [70] reported that the adsorbed H_2 over the oxidized Pd supported on alumina does not play any role in the reaction when only Pd is present on the catalyst surface. Additionally, Cu addition lowered the peak temperature of reduction over the catalysts, as measured by the TPR test. The surface reaction occurs following the L-H single site mechanism with the reaction between the adsorbed reactants to form adsorbed OH and eventually adsorbed H_2O (reactions 14-16). Johansson et al. [71] reported that both reactions 15 and 16 take place on the surface; however, reaction 15 is more dominant since the measurements for the peak intensities of OH desorption and water production do not match. The product H_2O then desorbs to the bulk stream inside the reactor (reaction 17). In this study, the rate law and reaction mechanism of the Pd-Cu catalyst for the CHC reaction have been proposed with high accuracy.

Table 7 compares the properties of the CHC catalyst developed and the activation energy of the CHC reaction over the developed catalyst in this study with those reported in the literature. The activation energy of the optimized catalyst, $Pd_{0.75}Cu_{0.25}/Al_2O_3$ (R600), was calculated as 22 kJ/mol by using an Arrhenius equation in the temperature range of 20-60 °C, which is lower than other alumina-supported Pd monometallic and Pd-Ni bimetallic catalysts. The comparison of the activation energies of catalysts for CHC is challenging since the catalyst composition, catalyst weight, and temperature range were different. Morfin et al. [31] calculated the

Table 6. CHC rate law parameters over the optimized catalyst for kinetic models 2-5

Kinetic models	k [μmol·g^{-1}·s^{-1}]	K_1 [bar^{-1}]	K_2 [bar^{-1}]	R^2
Kinetic model 2 (E-R H_2 adsorbed)	44.74	10,200	7,559	0.951
Kinetic model 3 (E-R O_2 adsorbed)	60.37	10,200	7,559	0.951
Kinetic model 4 (L-H single site)	1,357.56	37	14	0.967
Kinetic model 5 (L-H double site)	377.75	171	13	0.954

Table 7. Catalyst property and activation energy of various catalysts for CHC

Reference	Catalysts	Catalyst composition	Catalyst weight [mg]	Temperature range [°C]	Activation energy [kJ·mol^{-1}]
This study	Pd-Cu/Al_2O_3	0.75 wt% Pd; 0.25 wt% Cu	50	20-60	22.02
[31]	Pd/Al_2O_3	0.92 wt%	2,000	70-140	36
[31]	Pt/Al_2O_3	1.78 wt%	2,000	40-90	41
[31]	($Pd_{65}Pt_{35}$)/Al_2O_3	1.41 wt% Pd; 1.38 wt% Pt	2,000	40-90	40
[31]	($Pd_{20}Pt_{80}$)/Al_2O_3	1.41 wt% Pd; 0.20 wt% Pt	2,000	70-110	44
[36]	Pd-Ni/Al_2O_3	2 wt% Pd; 0.122 wt% Ni	100	25-70	39
[34]	Pd/Al_2O_3	0.5 wt%	30,000	35-85	73.8
[72]	Co_3O_4-ZrO_2	-	50	180-210	34.3
[72]	Pt/Co_3O_4-ZrO_2	2 at%	25	30-60	39.3
[72]	Pd/Co_3O_4-ZrO_2	2 at%	25	30-60	13.4
[74]	Pt/SiC	0.27 wt%	50	25-50	35
[64]	Pt/SiC	0.5 wt%	100	25-65	16
[73]	$Ti_{0.97}Pd_{0.03}O_{2-\delta}$	3 at%	110	20-120	32.6

activation energy of Pt, Pd, and Pt-Pd catalysts at low temperatures ranging between 36-44 kJ/mol. Lomot et al. [36,50] reported catalytic reactivity of alumina-supported Pd-Ni catalysts with the different elemental compositions of Pd and Ni. The Pd-Ni bimetallic catalysts showed higher reactivity than monometallic Pd catalysts, and 39 kJ/mol was the lowest activation energy. The activation energy of 73.8 kJ/mol calculated for 0.5%Pd/Al_2O_3 was higher than other catalysts as the size of alumina particles was 3-5 mm in diameter (40-160 μm in this study) [34]. The activation energy of Pd-based catalysts prepared by different preparation methods such as the sonochemical method [72] and solution combustion method [73] was also compared. The activation energy of Pd/Co_3O_4-ZrO_2 was 13.4 kJ/mol, where the substitution of Pd in the support resulted in effective H_2 and O_2 activation.

CONCLUSIONS

The impacts of metal composition and reduction temperature on the catalytic reactivity of alumina-supported Pd-Cu bimetallic catalysts during CHC were investigated in this study to optimize the catalyst composition, calculate the kinetic parameters, and develop the reaction rate law. The key findings are as follows:

(1) The reduced Pd-Cu catalysts show superior performance compared to the calcined Pd-Cu catalysts and enable CHC reaction at temperatures as low as 20 °C. The active metal particle sizes of the reduced Pd-Cu catalysts were smaller than those of the calcined catalysts, resulting in improved catalytic activity. The $Pd_{0.75}Cu_{0.25}$/Al_2O_3 catalyst exhibited the smallest active metal size (4.09 nm) and the highest reducibility among all catalysts tested.

(2) At elevated reduction temperatures, the Pd^0/Pd_{total} ratio increased while the active metal particle size decreased, reaching 43.25% and 4.09 nm, respectively. One contributing factor was believed to be the support-metal interactions, which resulted in the transfer of electrons from the reduced cations of the support to the dispersed metal ions. These changes to the catalyst structure promoted catalytic reactivity during the CHC. The optimized catalyst, $Pd_{0.75}Cu_{0.25}/Al_2O_3$ (R600) achieved a complete H_2 conversion at temperatures as low as 60 °C, which was retained for 40 h at the reaction temperature, showing superior catalyst stability.

(3) Based on the reaction rates measured at 60 °C, various kinetic models were compared to determine the most suitable model. The L-H single-site mechanism in which both Pd and Cu participate in the adsorption of H_2 and O_2 was determined as the most accurate rate law (R^2=0.967) with the highest kinetic constant. The reaction mechanism included the dissociative adsorption of H_2 and O_2, the surface reaction of adsorbed reactants forming adsorbed OH and then H_2O, and then the desorption of H_2O. The activation energy of the optimized catalyst during the CHC reaction was calculated as 22.02 kJ/mol, which is lower than other alumina-supported Pd monometallic and Pd-Ni bimetallic catalysts.

The findings of this study can be used for catalyst selection and reactor design for safer management of hydrogen-utilization systems, such as fuel-cell off-gas treatment and passive autocatalytic recombination in nuclear power plants.

ACKNOWLEDGEMENTS

This study was supported by the Australian Research Council (ARC) Discovery grant (DP210103025). We acknowledge the PhD scholarship from the University of Newcastle through the Australian Government Research Training Program Scholarship. The authors acknowledge the help and support from Dr Huiming Zhang for TEM-EDS analysis, Mr. Tony Rothkirch for ICP-MS tests, and Dr. Sathish Clastinrusselraj Indirathankam for TPR tests at the University of Newcastle.

ABBREVIATIONS

BET : Brunauer-Emmett-Teller
CHC : catalytic hydrogen combustion
EDS : energy-dispersive X-ray spectroscopy
E-R : Eley-Rideal
FWHM : full width at half maximum
HRTEM : high-resolution transmission electron microscopy

L-H : Langmuir-Hinshelwood
RT : room temperature
SMSI : strong metal support interaction
TCD : thermal conductivity detector
TPD : temperature-programmed desorption
TPR : temperature-programmed reduction
ICP-MS : inductively coupled plasma mass spectrometry
XPS : X-ray photoelectron spectroscopy
XRD : X-ray diffraction

DECLARATION OF COMPETING INTEREST

The authors declare that they have no known competing financial interests or personal relationships that could have appeared to influence the work reported in this paper.

REFERENCES

1. A. Kulkarni, S. Siahrostami, A. Patel and J. K. Nørskov, *Chem. Rev.*, **118**, 2302 (2018).
2. I. Staffell, D. Scamman, A. Velazquez Abad, P. Balcombe, P. E. Dodds, P. Ekins, N. Shah and K. R. Ward, *Energy Environ. Sci.*, **12**, 463 (2019).
3. Z. He, Y. Yan, F. Xu, Z. Yang, H. Cui, Z. Wu and L. Li, *Int. J. Hydrogen Energy*, **45**, 5014 (2020).
4. A. Cappelletti and F. Martelli, *Int. J. Hydrogen Energy*, **42**, 10513 (2017).
5. C. E. Arrieta, A. M. García and A. A. Amell, *Int. J. Hydrogen Energy*, **42**, 12669 (2017).
6. S. Malyshenko, *Int. J. Hydrogen Energy*, **29**, 589 (2004).
7. S. M. Brković, V. M. Nikolić, M. P. Marčeta Kaninski and I. A. Pašti, *Int. J. Hydrogen Energy*, **44**, 13364 (2019).
8. K. Park, H. Matsune, M. Kishida and S. Takenaka, *Int. J. Hydrogen Energy*, **42**, 18951 (2017).
9. R. He, G. Xu, Y. Wu, K. Shi, H. Tang, P. Ma, J. Zeng, Y. Bai and S. Chen, *Int. J. Hydrogen Energy*, **44**, 5940 (2019).
10. K. Park, T. Ohnishi, M. Goto, M. So, S. Takenaka, Y. Tsuge and G. Inoue, *Int. J. Hydrogen Energy*, **45**, 1867 (2020).
11. Q. Lu, J. Pan, S. Hu, A. Tang and X. Shao, *Int. J. Hydrogen Energy*, **41**, 12387 (2016).
12. J. Wan, A. Fan, K. Maruta, H. Yao and W. Liu, *Int. J. Hydrogen Energy*, **37**, 19190 (2012).
13. H. Yilmaz, *Int. J. Hydrogen Energy*, **44**, 25985 (2019).
14. V. F. Valdés-López, T. Mason, P. R. Shearing and D. J. L. Brett, *Prog. Energy Combust. Sci.*, **79**, 100842 (2020).
15. S. Wang, L. Chen, F. Niu, D. Chen, L. Qin, X. Sun and Y. Huang, *Int. J. Energy Res.*, **40**, 1979 (2016).
16. A. Qamareen, S. S. Alam and M. A. Ansari, *Energy Technol.*, **9**, 2100294 (2021).
17. Y. Yan, Q. Xu, W. Tang, Q. Huang, L. Zhang, L. Li and Z. Yang, *Energy Technol.*, **5**, 1495 (2017).
18. W. C. Pfefferle and L. D. Pfefferle, *Prog. Energy Combust. Sci.*, **12**, 25 (1986).
19. B. Fumey, S. Stoller, R. Fricker, R. Weber, V. Dorer and U. F. Vogt, *Int. J. Hydrogen Energy*, **41**, 7494 (2016).
20. B. Fumey, T. Buetler and U. F. Vogt, *Appl Energy*, **213**, 334 (2018).
21. B. Sarkar, R. R. Ratnakar and V. Balakotaiah, *Chem. Eng. J.*, **425**, 130318 (2021).
22. A. Q. Zade, M. Renksizbulut and J. Friedman, *Chem. Eng. J.*, **181-182**, 643 (2012).
23. Q. Huang, W. Li, Q, Lin, X. Zheng, H. Pan, D. Pi, C. Shao, C. Hu and H. Zhang, *J. Energy Inst.*, **91**, 733 (2018).
24. A. Setiawan, E. M. Kennedy, B. Z. Dlugogorski, A. A. Adesina, O. Tkachenko and M. Stockenhuber, *Energy Technol.*, **2**, 243 (2014).
25. J. K. Nørskov, J. Rossmeisl, A. Logadottir, L. Lindqvist, J. R. Kitchin, T. Bligaard and H. Jónsson, *J. Phys. Chem. B*, **108**, 17886 (2004).
26. J. F. Kramer, S.-A. S. Reihani and G. S. Jackson, *Proc. Combust. Inst.*, **29**, 989 (2002).
27. P. A. Deshpande and G. Madras, *Appl. Catal. B*, **100**, 481 (2010).
28. H.-J. Eom, J. H. Jang, D.-W. Lee, S. Kim and K.-Y. Lee, *J. Mol. Catal. A Chem.*, **349**, 48 (2011).
29. V. M. Shinde and G. Madras, *Catal. Today*, **198**, 270 (2012).
30. K. R. Kim, S. W. Paek, H. J. Choi and H. Chung, *J. Ind. Eng. Chem.*, **7**, 116 (2001).
31. F. Morfin, J.-C. Sabroux and A. Renouprez, *Appl. Catal. B*, **47**, 47 (2004).
32. Y. Iwai, K. Sato, J. Taniuchi, H. Noguchi, H. Kubo, N. Harada, Y. Oshima and T. Yamanishi, *J. Nucl. Sci. Technol.*, **48**, 1184 (2011).
33. K. K. Sanap, S. Varma, D. Dalavi, P. S. Patil, S. B. Waghmode and S. R. Bharadwaj, *Int. J. Hydrogen Energy*, **36**, 10455 (2011).
34. K. C. Sandeep, R. Bhattacharyya, C. Warghat, K. Bhanja and S. Mohan, *Int. J. Hydrogen Energy*, **39**, 17906 (2014).
35. E. Lalik, R. Kosydar, R. Tokarz-Sobieraj, M. Witko, T. Szumełda, M. Kołodziej, W. Rojek, T. Machej, E. Bielańska and A. Drelinkiewicz, *Appl. Catal. A*, **501**, 27 (2015).
36. D. Lomot and Z. Karpiński, *Res. Chem. Intermed.*, **41**, 9171 (2015).
37. V. N. Nguyen, R. Deja, R. Peters, L. Blum and D. Stolten, *Int. J. Hydrogen Energy*, **43**, 17520 (2018).
38. S. Yu, D. Hong, Y. Lee, S. Lee and K. Ahn, *Renew. Energy*, **35**, 1083 (2010).
39. Z. R. Ismagilov, M. A. Kerzhentsev, V. A. Sazonov, L. T. Tsykoza, N. V. Shikina, V. V. Kuznetsov, V. A. Ushakov, S. V. Mishanin, N. G. Kozhukhar, G. Russo and O. Deutschmann, *Korean J. Chem. Eng.*, **20**, 461 (2003).
40. A. E. Kozhukhova, S. P. Du Preez and D. G. Bessarabov, *Int. J. Hydrogen Energy*, **47**, 12726 (2002).
41. W. T. Figueiredo, G. B. Della Mea, M. Segala, D. L. Baptista, C. Escudero, V. Pérez-Dieste and F. Bernardi, *ACS Appl. Nano Mater.*, **2**, 2559 (2019).
42. M. Haruta and H. Sano, *Int. J. Hydrogen Energy*, **6**, 601 (1981).
43. V. M. Shinde and G. Madras, *Appl. Catal. B*, **132-133**, 28 (2013).
44. J.-W. Jung, K. Oh, K.-D. Jung, W. I. Kim and H. L. Koh, *Korean J. Chem. Eng.*, **38**, 1197 (2021).
45. S. Kaneko, T. Arakawa, M.-A. Ohshima, H. Kurokawa and H. Miura, *Appl. Catal. A*, **356**, 80 (2009).
46. F. Giarratano, G. M. Arzac, V. Godinho, D. Hufschmidt, M. C. Jiménez De Haro, O. Montes and A. Fernández, *Appl. Catal. B*, **235**, 168 (2018).
47. E. Lalik, A. Drelinkiewicz, R. Kosydar, R. Tokarz-Sobieraj, M. Witko, T. Szumełda, J. Gurgul and D. Duraczyńska, *Appl. Catal. A*, **517**, 196 (2016).
48. G. J. Kim, J. H. Shin and S. Chang Hong, *Int. J. Hydrogen Energy*,

45, 17276 (2020).
49. H. Roozbahani, S. Maghsoodi, B. Raei, A. S. Kootenaei and Z. Azizi, *Korean J. Chem. Eng.*, **39**, 586 (2022).
50. D. Lomot and Z. Karpiński, *Pol. J. Chem. Technol.*, **18**, 15 (2016).
51. Z. Yin, D. Gao, S. Yao, B. Zhao, F. Cai, L. Lin, P. Tang, P. Zhai, G. Wang, D. Ma and X. Bao, *Nano Energy*, **27**, 35 (2016).
52. S. R. Chowdhury, P. Mukherjee and S. K. Bhattachrya, *Int. J. Hydrogen Energy*, **41**, 17072 (2016).
53. J. Wu, S. Shan, J. Luo, P. Joseph, V. Petkov and C.-J. Zhong, *ACS Appl. Mater. Interfaces*, **7**, 25906 (2015).
54. M. B. Boucher, B. Zugic, G. Cladaras, J. Kammert, M. D. Marcinkowski, T. J. Lawton, E. C. H. Sykes and M. Flytzani-Stephanopoulos, *Phys. Chem. Chem. Phys.*, **15**, 12187 (2013).
55. J. Kim, J. Yu, S. Lee, A. Tahmasebi, C.-H. Jeon and J. Lucas, *Int. J. Hydrogen Energy*, **46**, 40073 (2021).
56. J. Papp, *J. Catal.*, **23**, 168 (1971).
57. S. M. A. Rahman, A. Tahmasebi, B. Moghtaderi and J. Yu, *Energy Fuels*, **34**, 6052 (2020).
58. G. J. Kim, D. W. Kwon and S. C. Hong, *J. Phys. Chem. C*, **120**, 17996 (2016).
59. Y. J. Huang, J. A. Schwarz, J. R. Diehl and J. P. Baltrus, *Appl. Catal.*, **37**, 229 (1988).
60. M.-k. Min, J. Cho, K. Cho and H. Kim, *Electrochim. Acta*, **45**, 4211 (2000).
61. A. P. Lagrow, M. R. Ward, D. C. Lloyd, P. L. Gai and E. D. Boyes, *J. Am. Chem. Soc.*, **139**, 179 (2017).
62. B. T. Meshesha, N. Barrabés, J. Llorca, A. Dafinov, F. Medina and K. Föttinger, *Appl. Catal. A*, **453**, 130 (2013).
63. J. Zheng, H. Zeng, C. Tan, T. Zhang, B. Zhao, W. Guo, H. Wang, Y. Sun and L. Jiang, *ACS Sustain. Chem. Eng.*, **7**, 15354 (2019).
64. G. M. Arzac, O. Montes and A. Fernández, *Appl. Catal. B*, **201**, 391 (2017).
65. V. S. Marakatti, S. C. Sarma, B. Joseph, D. Banerjee and S. C. Peter, *ACS Appl. Mater. Interfaces*, **9**, 3602 (2017).
66. Y. Liu, Y. He, D. Zhou, J. Feng and D. Li, *Catal. Sci. Technol.*, **6**, 3027 (2016).
67. M. Lesiak, M. Binczarski, S. Karski, W. Maniukiewicz, J. Rogowski, E. Szubiakiewicz, J. Berlowska, P. Dziugan and I. Witońska, *J. Mol. Catal. A: Chem.*, **395**, 337 (2014).
68. E. Garbowski and M. Primet, *J. Chem. Soc., Chem. Commun.*, **1**, 11 (1991).
69. H. S. Fogler, Pearson Education (1999).
70. M. G. Jones and T. G. Nevell, *J. Catal.*, **122**, 219 (1990).
71. Å. Johansson, M. Försth and A. Rosén, *Surf. Sci.*, **529**, 247 (2003).
72. S. A. Singh, K. Vishwanath and G. Madras, *ACS Appl. Mater. Interfaces*, **9**, 19380 (2016).
73. B. D. Mukri and M. S. Hegde, *Chem. Sci. J.*, **129**, 1363 (2017).
74. A. Fernández, G. M. Arzac, U. F. Vogt, F. Hosoglu, A. Borgschulte, M. C. Jiménez De Haro, O. Montes and A. Züttel, *Appl. Catal. B*, **180**, 336 (2016).